Eur. Phys. J. D (2023)77:157
https://doi.org/10.1140/epjd/s10053-023-00721-6

THE EUROPEAN PHYSICAL JOURNAL D

Regular Article – Atomic and Molecular Collisions

Dissociative electron attachment and dissociative ionization of $CF_3AuCNC(CH_3)_3$, a potential FEBID precursor for gold deposition

Ali Kamali[1], Will G. Carden[2], Jodie V. Johnson[2], Lisa McElwee-White[2], and O. Ingólfsson[1,a]

[1] Science Institute and Department of Chemistry, University of Iceland, Dunhagi 3, 107 Reykjavík, Iceland
[2] Department of Chemistry, University of Florida, Gainesville, FL 32611-7200, USA

Received 10 May 2023 / Accepted 27 June 2023

Abstract. Appreciable effort is currently committed to designing suitable organometallic precursors for fabrication of metallic nanostructures with focused electron beam induced deposition (FEBID)—a direct write method with high potential for 3D patterning. In this context, the initial interaction of the potential precursor with low energy electrons is critical and the extent of electron-induced ligand loss determines the composition of the resulting deposits. Specifically of interest are gold-containing precursors, as the optoelectronic properties of gold provide potential for a variety of plasmonic and light enhancing applications of 3D nanostructures. Here, we study low energy electron-induced fragmentation of $CF_3AuCNC(CH_3)_3$ through dissociative ionization (DI) and dissociative electron attachment (DEA) in the gas phase under single collision conditions and under conditions where collisional stabilization is provided. We further compare the fragmentation patterns observed under these conditions with the composition of deposits formed from this precursor under FEBID conditions. In DI, a significant difference in relative intensities is found under single collision conditions as compared to conditions where collisional stabilization is provided, while under both these conditions, only the same DEA channel is open. Comparison with the composition of deposits formed under FEBID conditions shows that the initial electron-induced fragmentation processes are not directly reflected in the deposit's composition. Rather, we expect these to determine the initial composition of immobilized fragments, while the final composition of the deposit is determined by electron-induced secondary and tertiary reactions caused by further irradiation after immobilization.

1 Introduction

Gold nanomaterials are employed in a wide variety of applications due to their unique optoelectrical properties. This is most noticeable in the biomedical sector where these have found application in, e.g., imaging, diagnostics, and cancer therapy [1–4], and a number of well controlled physical and chemical protocols have been developed for their fabrication [5–7]. Well defined 3D nanostructures also have high potential as passive and/or active elements in technological applications [8, 9]. For gold specifically, these include optical and electric sensors [10], surface enhanced Raman spectroscopy (SERS) elements [11], and plasmonic devices in general [12]. For the functionality of such stationary 3D nanostructures, however, their positioning, size, shape, and elemental purity are critical.

Focused Electron Beam Induced Deposition (FEBID) [13–15] is a direct write approach that has the potential of such control in the fabrication of free-standing nanostructures. In FEBID, a precursor gas enters an electron microscope through a gas injection system (GIS) in close proximity to a substrate surface where the precursor molecules are physisorbed in dynamic equilibrium

Reminiscence of good times More than one article could be written about Michael Brunger, the Hippy, and they would all be a testimony of a memorable man, a good scientist and more importantly a humorous, tolerant, and a very good person, moreover, they would be fun to read. However, in his spirit, I'm going to keep it short.
I was so fortunate to enjoy Michael's friendship, and his support and collaboration in science, in science administration (politics :-) and in personal matters. He also became dear to my children, when he generously hosted me and my family in Adelaide during my sabbatical in 2012, an experience we still talk about at the dinner table, now more than 10 years later. In one of our more personal conversations about lost ones, Michal said „*...as long as you are still talked about, you are not gone.*". With all the opportunities the Hippy has provided for reminiscence of good times, there is no doubt that many will talk kindly and of respect of him long time from now.
Oddur

T.I.: Electron and Positron Interactions and Their Applications-a tribute to Professor Michael Brunger. Guest editors: Márcio Henrique Franco Bettega, Stephen Buckman, Dragana Maric, Sylwia Ptasinska, Ron White.
[a] e-mail: odduring@hi.is (corresponding author)

Published online: 16 August 2023

with their gas phase. For metal deposition, such precursors are typically organometallic compounds with the central metal atom being that of the desired deposit [16]. A tightly focused, high-energy electron beam is directed at the surface, close to the gas injection point, and ideally the precursor molecules dissociate volatile ligands that are pumped away while the central atom(s) stays on the surface to build a pure metal deposit [17]. The lateral control of the shape of the structures created in this way is achieved by moving the electron beam relative to the surface of the substrate, and the vertical control is achieved by variation of the dwell time [13, 14]. However, composition control has proven to be difficult in FEBID, and generally significant amounts of impurities are found to be co-deposited with the desired metal element [18]. This is mainly due to incomplete decomposition of the precursor molecules under the electron beam, but adsorption and further decomposition of dissociated ligands and co-deposition of impurities from the background gas also play a role.

The general criteria for good precursors are that they are sufficiently volatile to be introduced to the FEBID system, that they are stable under ambient conditions, easy to handle, preferably of low toxicity, and commercially available [16, 19]. Most importantly, however, to achieve high purity depositions, the precursor molecules need to dissociate efficiently under the electron beam and the dissociated ligands need to readily desorb from the surface [16]. As a large variety of commercially available precursors for chemical vapor deposition (CVD) fulfill most of these criteria, most of the early reported FEBID experiments focused on depositions from these precursors. However, while CVD is thermally driven, in FEBID the fragmentation processes and thus the deposition, is electron driven [16, 17]. Moreover, significant numbers of secondary electrons are produced in inelastic scattering of the primary electrons from the substrate and forming deposits. Thus, the actual energy of the electrons inducing the fragmentation processes in FEBID is not that of the primary electrons alone. Rather, it is a distribution also reflecting the energy spread of the inelastic scattered and secondary electrons [20]. This energy distribution generally peaks below 10 eV and has a significant contribution close to 0 eV and a tail toward higher energies [20, 21]. To further complicate the situation, these electrons may cause dissociation of the precursor molecules through four distinct processes: dissociative ionization (DI), dissociative electron attachment (DEA), and neutral and dipolar dissociation (ND and DD) upon electronic excitation [20, 21]. These processes all have different energy dependences and lead to different fragmentation products, making the effective damage yield dependent on both the electron energy distribution and the energy dependence of the cross sections for the individual processes [20, 22, 23]. With this in mind, it is clearly a challenging task to design precursors that fragment completely under electron exposure and leave behind high metal content deposits.

Until fairly recently, the bulk of the studies on FEBID of gold were conducted with commercially available β-diketonate-derived Au(III) complexes commonly used in CVD, i.e., $Me_2Au(acac)$, $Me_2Au(tfac)$, and $Me_2Au(hfac)$ [24–27]. These are volatile and stable precursors; however, in FEBID without any purification steps, they generally deliver deposits with gold content ranging from 20 to 40 atom % and correspondingly high carbon content. This was addressed in a few studies by in situ or post-deposition oxidative removal of the carbon using oxygen or water, resulting in gold content as high as 81–92 atom %. [28]. In contrast to the Au(III) complexes, early experiments with the gold(I) complexes Cl–Au–PF_3 [29–31] and Cl–Au–CO [32] were found to produce high purity deposits without any purification measures. In these studies, 95 atom % Au was reported for Cl–Au–PF_3 [29–31] and the formation of gold grains with about 22 μΩ resistivity was reported for Cl–Au–CO [32]. However, these compounds are labile and readily decompose under ambient conditions, making them unsuitable for practical applications. Motivated by the high gold content of these precursors, efforts have been made to design stable and volatile gold(I) complexes that still maintain the high performance observed for Cl–Au–PF_3 and Cl–Au–CO in FEBID [16, 19, 33]. However, though these were generally found to be suitable FEBID precursors with respect to their volatility, stability, and deposit growth rates, the achievable gold content was low (about 7–22%), with the highest gold content (22%) achieved for $CF_3AuCNCH_3$ in deposition using an Auger spectrometer under UHV conditions [34].

Evidently FEBID involves a complex interplay between the fundamental electron-induced processes leading to the initial precursor fragmentation, electron-induced secondary processes, and how these are altered at surfaces and in the deposition process. It is thus important in the effort to tailor organometallic precursors for the use in FEBID, to understand the fundamental processes leading to their initial fragmentation and immobilization in the deposition process.

In this context, we have studied DEA and DI of $CF_3AuCNC(CH_3)_3$, one of the precursors from the series of recently tested Au(I) precursors [34]. Electron-induced fragmentation processes are studied in the gas phase under single collision conditions and under conditions where collisional stabilization is provided, i.e., conditions that should better reflect the effective energy dissipation that is in place at the surfaces in the FEBID process. Appearance energies are determined for selected DI processes, and quantum chemical calculations are used to support the interpretation of the observed DEA and DI processes. The gas phase results are compared to the composition of deposits from this precursor generated in an UHV Auger spectrometer [34] and discussed in the context of the initial fragmentation processes and electron-induced secondary decomposition.

2 Methods

2.1 Experimental setup

Electron-molecule interaction experiments under single collision conditions were carried out in a crossed beam instrument that has previously been described in detail [35]. A molecular beam of $CF_3AuCNC(CH_3)_3$ was generated by gas effusion through a stainless-steel capillary system that can be heated to achieve sufficient working pressure with low vapor pressure compounds. The effusive molecular beam crosses a quasi-monoenergetic electron beam that is generated with a trochoidal electron monochromator. Charged products that are formed in the interaction section are extracted into a quadrupole mass spectrometer (EPIC 1000, Hiden Analytical Warrington, UK) for m/z analyses and detection. The base pressure of the instrument was on the order of 2–4 $\times$ 10^{-8} mbar, and the electrostatic lens components are maintained at 393 K to avoid condensation of the target gas and background impurities. The working pressure during experiments was on the order of 2–4 $\times$ 10^{-7} mbar. In negative ion mode, the energy scale was calibrated by the peak of the SF_6^- formation from SF_6 set as 0 eV. The full width at half maximum of the same signal was used to estimate the energy resolution of the electron beam, which was found to be around 190 meV during the current experiments. The monochromator settings were kept the same for the positive ion measurements, and we assume the energy resolution to be the same. The energy scale in positive ion mode was calibrated by the first ionization energy of Ar, using the onset of the Ar^+ signal recorded in the beginning and end of each measurement day. Mass spectra were recorded at fixed incident electron energies by scanning through the relevant m/z range and ion yield curves were recorded at fixed m/z ratios by scanning through the relevant electron energy range. Appearance energies for the observed positive ions were determined by fitting a Wannier-type threshold function to the onset region of the respective ion yields. The reported AEs are the average of three measurements taken on different days, and the confidence limits are the standard deviations of the averages from these curves and are optical inspection to make sure that they bracket the onset of the individual curves. More information on the fitting procedure may be found in reference [36]. The intensities of the ion yields are normalized with respect to the working pressure and the ion signal from SF_6^- at 0 eV and Ar^+ at 70 eV for the negative and positive ions, respectively.

Direct insertion probe negative chemical ionization mass spectra (DIP NCI MS) and direct insertion probe electron ionization mass spectra (DIP EI MS) were recorded with a Thermo Scientific DSQ II equipped with a Thermo Scientific direct insertion probe (DIP). The spectra were recorded at an ion source temperature of 60C (373 K), and Qual Browser, Thermo Xcalibur 2.2 SP1.48, August 12, 2011, was used for data reduction. After evacuation of the sample vessel, the probe was held at 30 °C for 10 s before being ramped 1 °C/s to 60 °C where the temperature was kept constant for 10 min. Electron ionization mass spectra were recorded at 70 eV electron energy. The negative ion spectra were also recorded with 70 eV initial electron energy, but in the presence of methane as moderation gas for thermalization of the electrons, i.e., these represent thermal electron attachment at 333 K. While recording the DIP NCI MS, the methane moderation gas was supplied to the ionization region to maintain a nominal pressure of 1 Torr. In this setup, an approximately 1 mm^2 aperture allows gas flow into the main chamber where the pressure is about 4.4 $\times$ 10^{-6} Torr during the experiments. With the 3.8 Å kinetic diameter of methane, and at 1 Torr, the mean free path in the ionization region is about 53 nm, which translates to a collision frequency of about 5 $\times$ 10^8 s^{-1} at 333 K. During the DIP EI MS, on the other hand, the ionization region is open at the top, providing an approximately 100 mm^2 aperture connecting the ionization region with the main chamber. During these experiments, the pressure measured at the ion gauge of the main chamber is about 3.3 $\times$ 10^{-7} Torr, and as the conductance of the ionization region to the main chamber is directly proportional to the area of aperture, we estimate the pressure in the ionization region during the acquisition of the DIP EI MS to be 0.75 mTorr. Assuming a 10 Å kinetic diameter of $CF_3AuCNC(CH_3)_3$, this translates to a mean free path of 10 µm and a collision frequency of 2.7 $\times$ 10^6 s^{-1} at 333 K. Though these considerations only give an estimate, it is clear that the DIP EI experiments are not conducted under single collision conditions.

The subject molecule, $CF_3AuCNC(CH_3)_3$, was synthesized according to a previously published procedure [34]. It is a white colored powder but was found to adapt a slight pinkish appearance after prolonged storage under ambient conditions, indicating minor decomposition and formation of gold nanoparticles. Thermogravimetric analysis, however, showed no sign of mass loss up to about 290 K, after which rapid mass loss is observed with 30% reduction reached at 310 K [37]. All samples were stored refrigerated at − 20 °C.

2.2 Quantum chemical calculations

All quantum chemical calculations were performed using the ORCA computational chemistry software, version 4.1 [38]. The geometry optimizations for all the neutral and charged fragments and parent molecules were performed with tight SCF settings using the hybrid DFT functional PBE0 as well as the triple-zeta polarization basis set def2-TZVP, and the D3BJ dispersion correction by Grimme et al. [39]. In addition, for closed-shell and open-shell systems, the unrestricted Kohn–Sham (UKS) and restricted Kohn–Sham (RKS) formalisms were used, respectively. The PBE0 functional was chosen based on studies by Kepp et al. [40] and Kang et al. [41], where they found it to be one of the most accurate functionals at predicting the binding energies and structures of gold complexes.

Harmonic vibrational frequencies were confirmed to be positive at the PBE0/def2-TZVP level of theory and were used to calculate the zero-point vibrational energy and thermal corrections. In addition to the DFT calculations, single point calculations were also conducted at the coupled-cluster level of theory on the optimized PBE0-TZVP geometries [42]. These calculations were carried out with normal PNO settings at the DLPNO-CCSD(T) level, using the double-zeta basis set def2-TZVP and the valence quadrupole-zeta auxiliary basis set TZVP/c.

The threshold values reported were calculated by subtracting the energy of all generated fragments from the energy of the parent molecule, including the zero-point vibrational energy and thermal corrections for the parent molecule and all fragments. For comparison with the experimental AEs, the threshold values for alternative reaction paths, leading to the observed m/z ratios, were calculated.

3 Results and discussion

Figures 1 and 2 show positive ion mass spectra of $CF_3AuCNC(CH_3)_3$ recorded at 70 eV electron Impact energy. The mass spectra in Fig. 1 show the m/z range from around 10 to about 190, i.e., covering fragments that do not contain the central Au metal atom (m/z 197), and Fig. 2 covers the m/z range from about 190 to about 360. In both figures, the mass spectra shown in panels (a), (b), and (c) are recorded in the crossed beam experiment with the capillary inlet system at 298, 333, and 353 K, respectively. For comparison, a direct insertion probe electron ionization mass spectrum (DIP EI MS) covering the same m/z ranges is shown in panel (d). Similarly, Fig. 3a–c shows negative ion mass spectra recorded in the crossed beam experiment at about 0 eV incident electron energy with the inlet system at 298, 333, and 353 K, respectively, while panel (d) shows a direct insertion probe chemical ionization negative ion mass spectrum (DIP NCI MS). Crossed beam MS for negative ions was also recorded at 1 eV intervals up to 10 eV, but no significant fragments were observed above 0 eV.

Most noticeably, the positive ion mass spectra (Figs. 1, 2) show a rich fragmentation pattern, while only the m/z ratios 292, $[CF_3AuCN]^-$, and m/z 335 are observed in the crossed beam negative ion mass spectra at 353 K, and m/z 292 is the only significant contribution in the DIP NCI spectrum. In fact, m/z 335 originates from an impurity caused by minor decomposition of the sample during shipping of the batch used in the crossed beam experiment and is attributed to the formation of $[Au(CF_3)_2]^-$. The same batch of material did not show this impurity before shipping as has been confirmed with DIP NCI MS performed at the University of Florida (Fig. 3d). Thus, $[CF_3AuCN]^-$ is the only significant ion formed from $CF_3AuCNC(CH_3)_3$ upon

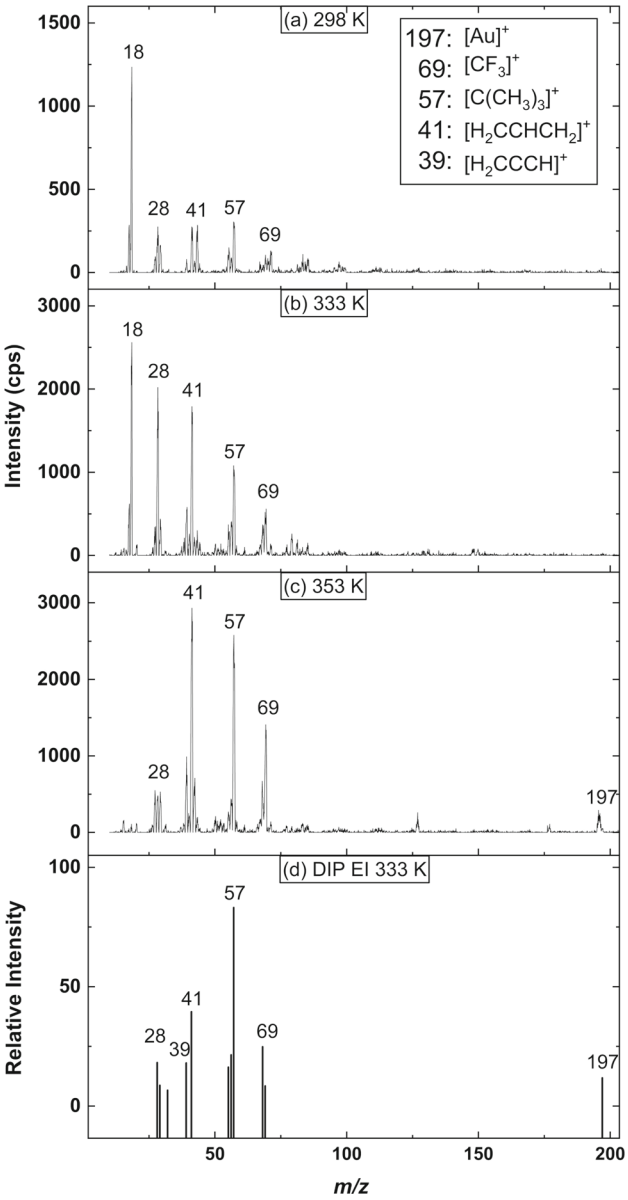

Fig. 1 Positive ion mass spectra of $CF_3AuCNC(CH_3)_3$, recorded at 70 eV electron impact energy. **a–c** Recorded in the crossed beam experiment in the m/z range of from 10 to 200 with the inlet system at 298 K, 333 K, and 353 K, respectively. **d** Recorded in the m/z range from 25 to 200, using direct insertion probe electron ionization mass spectrometry (DIP EI MS) at a probe temperature of 333 K

electron attachment. For the positive ions, it is apparent in the comparison of the crossed beam mass spectra with the DIP EI spectrum that the relative intensities of the low m/z fragments are significantly higher in the crossed beam experiment. At the lower temperatures, this is to a large extent due to background impurities in the crossed beam chamber and minor decomposition during shipping, as is apparent when comparing the crossed beam spectra recorded at room temperature,

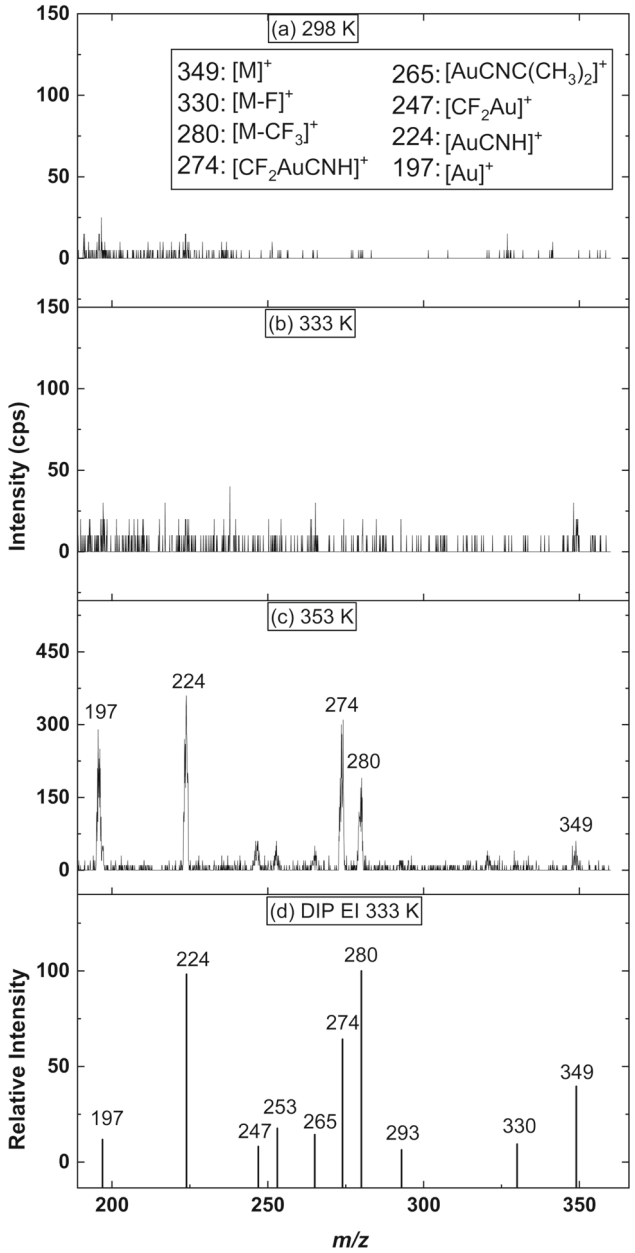

Fig. 2 Positive ion mass spectra of $CF_3AuCNC(CH_3)_3$, recorded at 70 eV electron impact energy over the m/z range from 190 to 360. **a–c** Recorded in the crossed beam experiment with the inlet system at 298 K, 333 K, and 353 K, respectively. **d** Recorded with the direct insertion probe electron ionization mass spectrometer (DIP EI MS) at a probe temperature of 333 K

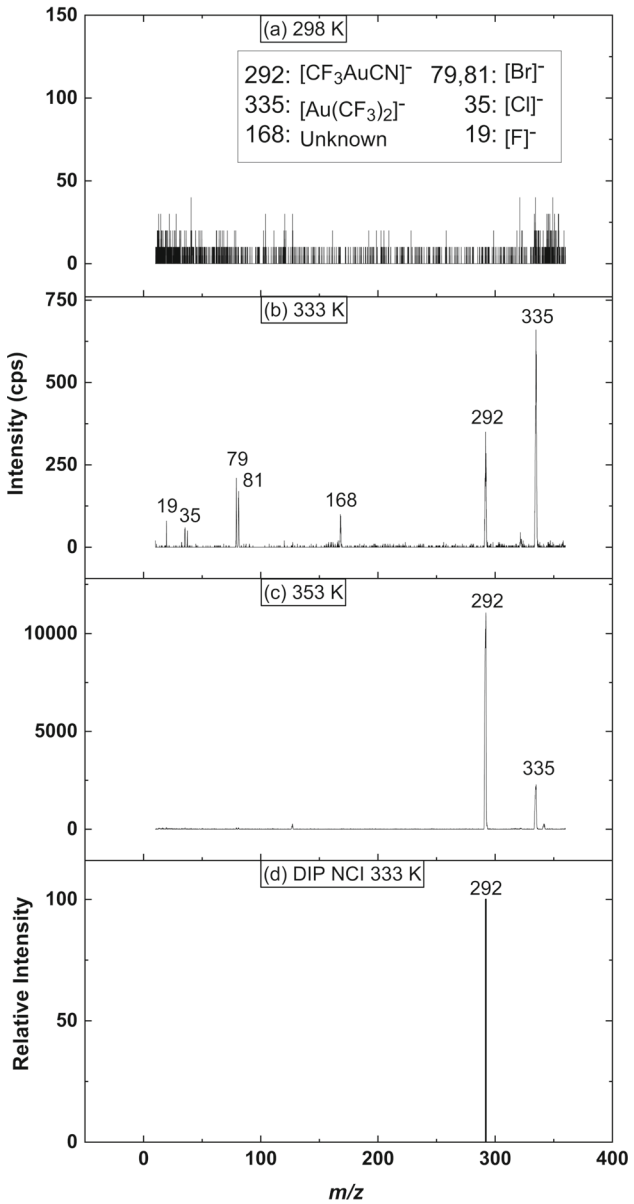

Fig. 3 Negative ion mass spectra of $CF_3AuCNC(CH_3)_3$. **a–c** Recorded in the crossed beam experiment at an incident electron energy of 0 eV in the m/z range from 10 to 360 with the inlet system at 298 K, 333 K, and 353 K, respectively. **d** Recorded using direct injection probe negative chemical ionization (DIP NCI MS) in the m/z range from 50 to 360, at a probe temperature of 333 K using methane at 1 torr nominal pressure as moderation gas

333 K and 353 K. However, the most significant contributions in the spectra recorded at 353 K, m/z 39, 41, 57, and 69 are clearly from DI of $CF_3AuCNC(CH_3)_3$. And, though we cannot exclude some contributions from thermal decomposition at 353 K, we consider this to be unlikely as the decomposition temperature of $CF_3AuCNC(CH_3)_3$ as determined by thermogravimetry, is 373 K. Furthermore, no significant changes in the MS were observed over several days of experiments. This is also apparent from the relative intensity of the m/z 335 peak in the crossed beam negative ion mass spectra recorded at 333 as compared to 353 K. We thus attribute the difference in the relative intensities observed in the 353 K crossed beam spectrum and the DIP EI spectrum, mainly to the fact that the local pressure in the ionization region of the DIP EI mass spectrometer is well beyond that for single collision conditions. Hence, collisional stabilization influences the relative intensities in the positive DIP mass spectra. This

effect may be further enhanced by the higher internal energy at 353 K as compared to 333.

Notwithstanding, with an estimated pressure in the ionization region of 0.75 mTorr, as discussed in the experimental section, the mean free path is on the order of 10 μm in the DIP EI MS experiment; hence, a number of collisions will take place on the ion's way from its site of ionization to the entrance of the mass spectrometer. The origin of the *m/z* 39, 41, 57 and 69 fragments from the intact parent molecule is further supported by comparing the experimental appearance energies (AEs) of these with the respective calculated thresholds for their formation through dissociative ionization of $CF_3AuCNC(CH_3)_3$. Figure 4 shows the onset region of the ion yield curves for these fragments along with the respective Wannier-type threshold fits used to determine their appearance energies (AEs). The optimized structures of the ionic fragments are also shown in the respective panels along with their AEs and confidence limits as determined from three independent data sets (see method section). Table 1 compares these AEs with the thermally corrected threshold energies calculated at the PBE0-def2-TZVP and DLPNO-CCSD(T)-def2-TZVP levels of theory for potential processes leading to their observation. In general, the DLPNO-CCSD(T)-def2-TZVP level of theory is considered to be the more accurate approach and in our assignments of the observed *m/z* ratios, we look for agreement with this method.

For *m/z* 39, the experimentally determined AE is found to be 15.0 ± 0.3 eV. This fragment must originate from partial fragmentation of the *t*-butyl isocyanide ligand, leading either to the elemental compositions C_3H_3 or NC_2H for the positive ion fragment. For this fragment, the best agreement with the threshold values is found for the formation of the $[H_2CCCH]^+$ cation and CF_3AuCN, CH_4, and H_2 as neutral fragments. At the PBE0-def2-TZVP and DLPNO-CCSD(T)/def2-TZVP levels of theory, the threshold for this reaction is found to be 15.32 and 14.87 eV, respectively. Assuming the formation of $[HCCHCH]^+$ rather than $[H_2CCCH]^+$ lowers the threshold values to 13.91 and 13.68 eV, respectively. This is in both cases more than 1 eV below the experimental AE. Considering the formation of $[CNCH]^+$ and the neutrals CF_3Au and propane ($CH_3CH_2CH_3$), on the other hand, results in threshold values of 15.65 and 15.48 eV, at the respective levels of theory. These are both about 0.5 eV above the experimental value for the AE of *m/z* 39.

For *m/z* 41, the AE is found to be 12.1 ± 0.3 eV, and the best agreement with the calculated threshold at the DLPNO-CCSD(T)/def2-TZVP level of theory is found when considering the formation of $[H_2CCHCH_2]^+$ and the neutral counterparts CH_4 and CF_3AuCN, where we find the AE to be 12.45 eV. At the PBE0-def2-TZVP level, the threshold for this reaction is found to be 12.65 eV, i.e., 0.25 eV above the higher confidence limit of the AE. However, considering the $[H_2CCCH_3]^+$ isomer as the positive fragment raises the threshold values to 12.85 and 12.82, respectively, i.e., about 0.4 eV above the higher confidence limit. Also, a number of isomers of C_2H_3N were considered for the positively charged fragment *m/z* 41, as is shown in Table 1. The threshold values for these were, generally found to be well above the experimental AE, with the exception of the formation of the $[HCNCH_2]^+$ ion and $CF_3AuC(CH_3)_2$ as the neutral counterpart. For this reaction, we find the threshold to be 12.35 eV at the PBE0-def2-TZVP level of theory, hence in good agreement with the experimental value, but at the coupled cluster level, the threshold is found to be 12.52 eV, about 0.2 eV above the confidence limits of the AE. This reaction, however, constitutes significant rearrangements including rupture of the CN triple bond and extensive rearrangement of the *t*-butyl group. We thus consider this channel unlikely as compared to the formation of $[H_2CCHCH_2]^+ + CH_4 + CF_3AuCN$ which constitutes single bond ruptures and hydrogen migration within the fragmenting *t*-butyl group.

For the *m/z* ratios 57 and 69, the assignment is more straight forward as these can unambiguously be assigned to $[C_4H_9]^+$ and $[CF_3]^+$, respectively. For *m/z* 57 the AE is found to be 10.3 ± 0.2 eV and for direct dissociation and the formation of $[C(CH_3)_3]^+$ and CF_3AuCN as the neutral counterpart the calculated threshold for this reaction is 10.61 and 10.82 eV at the PBE0-def2-TZVP and DLPNO-CCSD(T)/def2-TZVP levels of theory, respectively. Hence, 0.1 and 0.3 eV above the confidence limit, respectively. We additionally considered the formation of $[HC(CH_2)(CH_3)_2]^+$ through hydrogen transfer from one of the methyl groups to the central carbon, but at both levels of theory, we find the threshold for this reaction to be more than 4 eV above the experimental AE. For *m/z* 69, i.e., the formation of $[CF_3]^+$ and $AuCNC(CH_3)_3$, the AE is found to be 12.3 ± 0.3 eV and threshold energies of 12.62 and 12.67 eV are calculated at the PBE0-def2-TZVP and DLPNO-CCSD(T)/def2-TZVP levels of theory, respectively. In both cases, these are only marginally above the upper confidence limit of the experimental AE.

In general, the agreement between the experimental AEs and the calculated threshold values is good, though the threshold values tend to be somewhat higher than the AEs, and more so at the DFT level of theory. This is likely, at least in part, to be due to the fact that the thermal correction is that of the average, and not the energy distribution at 353 K. Thus, the high-energy tail of the distribution may shift the observed AEs to lower energies with respect to the actual thermally corrected thresholds.

As shown in Fig. 2, the main gold-containing fragments in the crossed beam experiment are observed at *m/z* 197, 224, 274, and 280, corresponding to the positive ions Au^+, $[AuCNH]^+$, $[CF_2AuCNH]^+$and $[AuCNC(CH_3)_3]^+$. Lesser contributions are observed at *m/z* 247, 253, and 265, and based on their elemental composition, stability and extent of rearrangement required for their formation, they are assigned to $[AuCF_2]^+$, $[CH_3AuCNCH_3]^+$, and $[AuCNC(CH_3)_2]^+$. A minor contribution is also observed from the parent cation $[CF_3AuCNC(CH_3)_3]^+$ at *m/z* 349. Qualitatively, this agrees with the *m/z* ratios observed in the

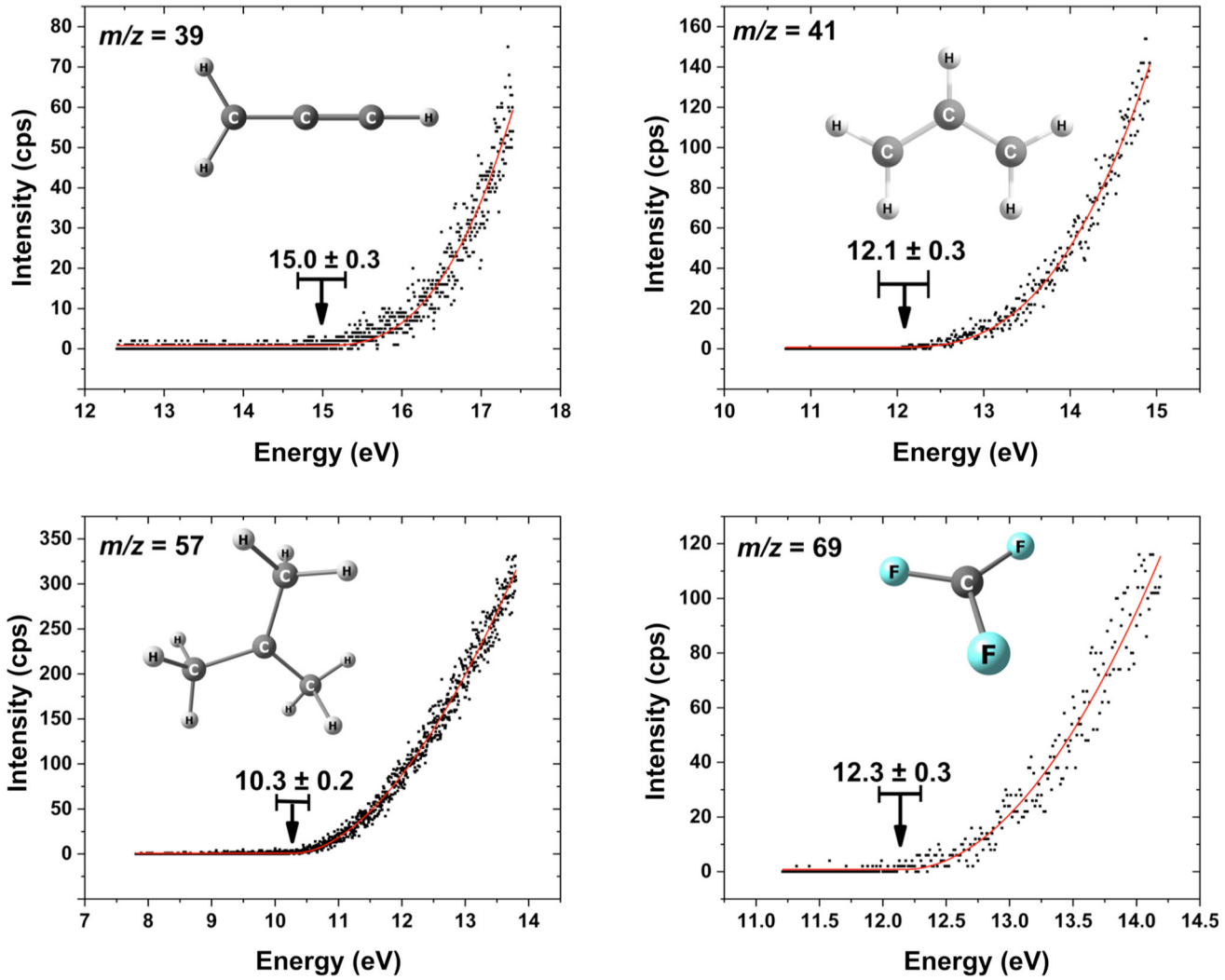

Fig. 4 Onset region of typical yield curves for m/z 39, 41, 57, and 69 along with the Wannier-type threshold fits used to determine their appearance energies (AEs). Also shown are the respective AEs and their confidence limits as determined from three measurements recorded on different days and the assigned fragment structures optimized at the PBE0-def2-TZVP level of theory

DIP EI spectra shown in panel d), however, the relative intensities differ markedly in these experiments. For further comparison, Table 2 compares the relative intensities of the main fragments observed in the crossed beam experiment with those observed in the DIP EI experiment. The intensities are normalized with respect to the highest intensity fragments set as 100 in both cases. In the crossed beam experiment, this is m/z 41; $[H_2CCHCH_2]^+$ and in the DIP EI, m/z 280; $[AuCNC(CH_3)_3]^+$. Additionally, the relative intensities of the gold-containing fragments observed in the crossed beam experiment experiments are shown in the last column, normalized to the highest intensity gold-containing fragment, m/z 224. With respect to the gold-containing fragments, it is most notable that the relative intensity of Au^+, m/z 197, is significantly higher in the crossed beam experiment as compared to the DIP EI MS. Conversely, the relative intensity of the parent cation is significant in the DIP EI MS, while it is only a minor contribution to the mass spectra recorded under single collision conditions. We attribute this to the effect of collisional stabilization in the DIP EI MS experiment. This can also explain the absence of m/z 330, $[CF_2AuCNC(CH_3)_3]^+$ and the relatively low intensity of m/z 280 in the crossed beam experiment under single collision conditions as compared to DIP EI MS, as both these fragments may decay further to form m/z 274 $[CF_2AuCNH]^+$, 247 $[CF_2Au]^+$, 224 $[AuCNH]^+$ or 197 $[Au]^+$.

A priori, one would expect that the DIP EI MS, where collisional stabilization is provided, should better reflect the fragmentation as it is observed at surfaces where an effective energy dissipation is in place. It is thus interesting to compare the current experiments with the composition of actual deposits formed

Table 1 For the $CF_3AuCNC(CH_3)_3$ precursor, the calculated threshold energies at the PBE0-TZVP and DLPNO-CCSD(T)-TZVP levels of theory were combined with the potential reaction pathways to determine the appearance energy (AE) values of the most significant ions observed in the mass spectra resulting from dissociative ionization (DI) and dissociative electron attachment (DEA). Additionally, the formation of each fragment was analyzed in detail

$CF_3AuCNC(CH_3)_3$				
m/z	Products	AE (eV)	PBE0-def2-TZVP (eV)	DLPNO-CCSD(T)-def2-TZVP (eV)
39	**$[H_2CCCH]^+$ + CF_3AuCN + CH_4 + H_2**	15.0 ± 0.3	**15.32**	**14.87**
	$[CNCH]^+ + CF_3Au + CH_3CH_2CH_3$		15.56	15.48
	$[HCCHCH]^+ + CF_3AuCN + CH_4 + H_2$		13.91	13.68
41	**$[H_2CCHCH_2]^+$ + CH_4 + CF_3AuCN**	12.1 ± 0.3	**12.65**	**12.45**
	$[CNCH_3]^+ + CF_3Au + CH_3CCH_3$		17.33	17.23
	$[CNCH_3]^+ + CF_3AuC(CH_3)_2$		14.67	14.47
	$[HCNCH_2]^+ + CF_3Au + CH_3CCH_3$		15.18	15.27
	$[HCNCH_2]^+ + CF_3AuC(CH_3)_2$		12.35	12.52
	$[H_2CCCH_3]^+ + CH_4 + CF_3AuCN$		12.85	12.82
57	**$[C(CH_3)_3]^+$ + CF_3AuCN**	10.3 ± 0.2	**10.61**	**10.82**
	$[HCCH_2(CH_3)_2]^+ + CF_3AuCN$		14.54	14.85
69	**$[CF_3]^+$ + $AuCNC(CH_3)_3$**	12.3 ± 0.3	**12.62**	**12.67**
292	**$[CF_3AuCN]^-$ + $C(CH_3)_3$**	0	**−1.20**	**−1.23**

The threshold values are calculated for different reaction paths and the assigned reaction, based on the best match with the DLPNO-CCSD(T)-TZVP threshold values, are highlighted bold. Additionally, the AE and the threshold values for the formation of *m/z* 292, $[CF_3AuCN]^-$, through dissociative electron attachment to $CF_3AuCNC(CH_3)_3$ are shown in the last row

Table 2 Normalized peak intensities from the EI mass spectra of $CF_3AuCNC(CH_3)_3$ at 70 eV recorded under single collision conditions and in DIP EI MS

m/z	Fragment	Relative intensity		
		Crossed beam	DIP	Au-fragments crossed beam
349	$[CF_3AuCNC(CH_3)_3]^+$	2	40	15
330	$[CF_2AuCNC(CH_3)_3]^+$	0	9	0
280	$[AuCNC(CH_3)_3]^+$	2	100	17
274	$[CF_2AuCNH]^+$	11	64	92
265	$[AuCNC(CH_3)_2]^+$	0	14	0
247	$[CF_2Au]^+$	2	8	17
224	$[AuCNH]^+$	12	98	100
197	$[Au]^+$	10	12	83
69	$[CF_3]^+$	48	8	-
57	$[C(CH_3)_3]^+$	88	83	-
41	$[H_2CCHCH_2]^+$	100	40	-
40	$[H_2CCCH_2]^+$	9	0	-
39	$[H_2CCCH]^+$	34	18	-
15	$[CH_3]^+$	5	-	-

The intensities are normalized with respect to the highest intensity fragment set as 100 in both cases. This is *m/z* 41 in the crossed beam experiment and *m/z* 280 in the DIP EI experiment (columns three and four, respectively). For better comparison, the last column also shows the relative intensities of gold-containing fragments observed in the crossed beam experiment normalized to the highest intensity gold-containing fragment, *m/z* 224

Table 3 Average carbon, fluorine, and nitrogen loss per incident observed in the crossed beam EI experiment, the DIP EI experiment and in DEA (crossed beam and DIP NCI)

Element loss	C		N		F
Crossed beam (EI)	3.15		0.03		0.71
DIP EI	3.30		0.04		1.71
DEA (Crossed beam and DIP)	4		0		0
Elemental composition calculated for EI and DEA and observed in EBID (Ref. [34])					
Crossed beam (EI)	14 at.% Au	40 at.% C	32 at.% F	14 at.% N	
DIP EI MS	17 at.% Au	45 at.% C	22 at.% F	16 at.% N	
DEA	14 at.% Au	29 at.% C	43 at.% F	14 at.% N	
EBID [34]	14 at.% Au	80 at.% C	0 at.% F	6 at.% N	< 1 at.% O

Also shown are the atomic compositions that would result from the respective average elemental losses and the deposits composition observed in EBID in an Auger spectrometer at an electron energy of 5 keV [34]

under FEBID conditions. In this context, Table 3 shows the average carbon, fluorine, and nitrogen loss per incident in the gas phase experiments, and the atomic composition of a hypothetical deposit that would result if these processes, unaltered, and alone, would determine the composition of a deposit. For the average element loss, the contribution of all gold-containing fragments is weighted with the respective number of carbons, fluorine, or nitrogen lost and divided by the total intensity of all fragments. For m/z 39, 41, 57, and 75, the neutral gold-containing fragments as assigned in Table 2 provide the basis for this calculation for both experiments. The elemental composition of a deposit formed from this precursor under FEBID conditions [34] is shown at the bottom of the table. These deposition experiments were conducted under UHV in an Auger spectrometer at an electron beam energy of 3 kV and a current of 1 μA on a silicon substrate that was pre-treated by sputtering with 4 keV Ar^+ ions to remove the oxide layer and residual carbon.

With this approach, the average F, N, and C loss per incident in the crossed beam experiment is found to be 0.71, 0.03, and 3.15, respectively, and in the DIP EI MS, these are found to be 1.71, 0.04, and 3.30, respectively. Under the assumption that all fragments that do not contain gold would desorb, this translated to a deposit of 14 at.% Au, 40 at.% C, 32 at.% F, and 14 at.% N using the crossed beam data. The expected composition derived from the DIP EI MS data, where collisional stabilization potentially plays a role, would be 17 at.% Au, 45 at.% C, 22 at.% F, and 16 at.% N, respectively. Applying the same approach to the negative ion data, where the only significant fragment is $[CF_3AuCN]^-$ (m/z 292) in both experiments is straightforward and results in an expected Au:C:F:N deposit composition of 1:2:3:1, i.e., 14 at.% Au, 29 at.% C, 43 at.% F, and 14 at.% N. For comparison, the elemental composition of the deposit generated under FEBID conditions was found to be 14 at.% Au, 80 at.% C, 0 at.% F and 6 at.% N, as determined by EDX [34]. Most noticeably, fluorine is as good as quantitatively removed in the deposition experiments, while less than 1 fluorine is lost on average per incident through DI under single collision conditions and 1.7 in the DIP EI experiments. Moreover, the fluorine loss in both the gas phase EI experiments is substantially through the loss of the CF_3 group from the central gold. This is clearly not the route for fluorine loss in the deposition experiment where no carbon removal is observed, and the stoichiometric Au:C ratio of the precursor is retained in the deposit. Furthermore, in DEA, both under single collision conditions and in the DIP NCI experiment, no fluorine loss is observed. It is thus clear that the DEA and DI processes observed in the gas phase are not reflected in the deposit's composition, even if collisional stabilization is provided. However, this is in line with the interpretation of the deposition experiments, where sequential fluorine loss upon prolonged irradiation of the initial deposit was proposed [34]. Considering that the electron dose in the deposition experiment was about 1.15×10^{14} $e^-/\mu m^2$, electron-induced secondary reactions are likely to play a significant role. Presuming, for simplicity, dense packing and a 1 nm^2 area occupied by each molecule at the surface, 1 μm^2 is covered by a monolayer of 10^6 molecules. The thickness of the deposit in the Auger experiments was stated to be > 100 nm, and if we, for sake of argument, assume 200 nm thickness, each molecule has been exposed to more than 5×10^5 electrons. With a generic electron-induced fragmentation cross section of 10^{-16} cm^2, which is on the order of magnitude determined for other FEBID precursors [22, 43, 44], the reactive area of this 1 μm^2 coverage is about 0.01 μm^2. Thus, each molecule may have been subject to about 5000 reactive incidences. In this consideration, it is assumed that the cross section remains the same after each reactive incident and that the reaction cross section of the high-energy primary beam is the same as measured with low energy electrons in the gas phase. These assumptions do not hold, and the cross sections for further electron-induced decomposition of immobilized secondary and tertiary fragments may be orders of magnitude lower than those for the initial process. Nonetheless, it is clear from these considerations that electron-induced

secondary reactions may play a significant, if not determining role in FEBID. It is also clear that the carbon containing ionic fragments do not desorb from the surface but are rather immobilized and subjected to further electron-induced fragmentation. Secondary and tertiary electron-induced reactions have been discussed in context to other FEBID precursors [23, 45] and is in fact reflected in a number of non-steady state experiments where thin precursor layers are exposed to 500 eV electrons, and the elemental composition change is monitored in dependence of the electron dose. Good examples are the precursors $Ru(CO)_4I_2$ [46], cis-$Pt(CO)_2Cl_2$ [47], and (η^3-C_3H_5)$Ru(CO)_3Br$ [48], where initial electron-induced carbonyl loss at low electron doses correlates well with low energy electron-induced fragmentation as it is observed in the gas phase. Continued electron exposure, however, leads to further, secondary fragmentation, partly resulting in removal (desorption) of the halogens but also in decomposition of carbon containing ligands and integration of carbon in the deposit.

Turning back to the negative ion formation, Fig. 5a shows the ion yield curve for $[CF_3AuCN]^-$ in the energy range from 0 to 10 eV, with an expanded insertion comparing the normalized $[CF_3AuCN]^-$ ion yield curve and that of SF_6^- from SF_6, used for the respective energy calibration. Figure 5b compares contour plots of the LUMO of the neutral molecule with the HOMO (SOMO) of the ground state anion. The contour plots are generated with Chemcraft [49] for the respective equilibrium geometries optimized at the PBE0-def2-TZVP level of theory and visualized with a contour value of 0.05. Noticeably, the $[CF_3AuCN]^-$ signal shown in Fig. 5a is slightly blue shifted (0.05 eV) and significantly broader (FWHM of 300 meV) than that of the SF_6^- ion yield (190 meV), which in turn, reflects the energy distribution of the electron beam. As discussed above, the DEA spectra recorded in the crossed beam experiment under single collision conditions and in DIP NCI are nearly identical, with the dominating contribution being from m/z 292, i.e., loss of the t-butyl group with the formation of $[CF_3AuCN]^-$. The only difference is the additional observation of a fairly weak $[M–H]^-$ signal (about 7%) in the DIP NCI spectra. This is not surprising as the DIP NCI experiments are recorded in the presence of methane as moderation gas at a pressure of about 1 torr (see the experimental section). The mean free path is thus on the order of 50 nm in these experiments, corresponding to a collisional frequency of about 5×10^8 s^{-1} at 333 K. This in turn provides for efficient collisional stabilization and observation of the relaxed ground state anion is expected. Furthermore, at the PBE0-def2-TZVP level of theory, we find the adiabatic electron affinity (EA) of $CF_3AuCNC(CH_3)_3$ to be 0.63 eV and thus, all prerequisites for the formation of the stable ground state anion should be provided. However, when comparing the vacant LUMO of the neutral with the HOMO of the

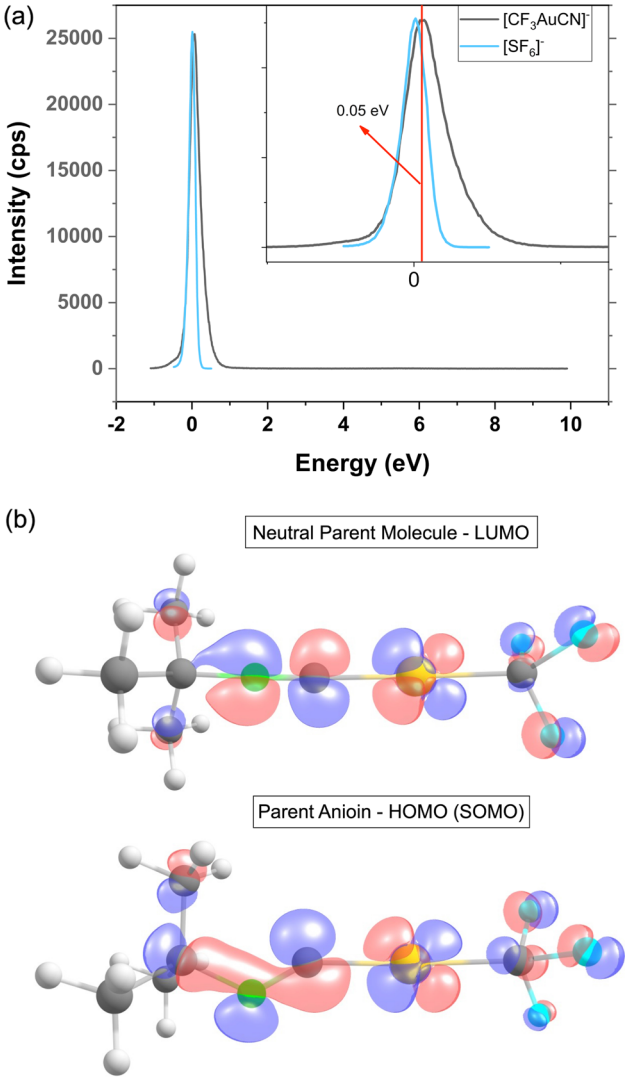

Fig. 5 **a** Ion yield curve of $[CF_3AuCN]^-$ formed in DEA to $CF_3AuCNC(CH_3)_3$ under single collision conditions in the incident electron energy range from about 0 to 10 eV. The inset shows an expansion of the energy range from about 0 to 1.5 eV, along with the respective $[SF_6]^-$ calibration curve. **b** Isosurfaces of the LUMO of the neutral $CF_3AuCNC(CH_3)_3$ molecule and the HOMO (SOMO) of its ground state anion. These are generated with Chemcraft for the respective relaxed geometries optimized at the PBE0-def2-TZVP level of theory

anion (Fig. 5b), it is clear that a single electron occupation of the LUMO of the neutral leads to strong coupling of this electronic state with the N–$C(CH_3)_3$ coordinate. While the neutral HOMO is antibonding with π^* character along the AuC–N coordinate of the linear ground state, a single electron occupation of this orbital leads to stabilization of the molecular anion through substantial bending of the C–N–C coordinate, leading to a change of the respective angle from 180° to 150°. Hence, the geometrical relaxation of the initially formed TNI to its ground state proceeds along a deformation

coordinate, while the dissociation leading to the formation of $[CF_3AuCN]^-$ is directly along the N–$C(CH_3)_3$ bond. It is also apparent, that strong orbital mixing is provided along the dissociation coordinate whereby the AuC–N antibonding π^* character of the LUMO of the neutral is largely lost. In turn, it acquires an admix of σ^* character along the N–$C(CH_3)_3$ bond with an antibonding node at the C atom in the fully relaxed geometry. From these considerations, we anticipate that the initial TNI formed in the vertical transition is a strongly repulsive state with orbital mixing provided in the attachment process through the N–$C(CH_3)_3$ bending motion. In this picture, the extension along the N–$C(CH_3)_3$ coordinate is fast compared to the relaxing bending motion and proceeds on a timescale shorter than the collisional stabilization provided in the DIP NCI experiments. From the fundamental physical and chemical point of view, this is an interesting dynamic problem that is worthy of further studies, both from the experimental and theoretical side. Specifically, angular dependence measurements of the attachment process, such as velocity imaging would be of interest. Also, on the theory side, non-adiabatic dynamic calculations would provide further insight. With respect to the deposition experiments discussed here above, these dynamics may offer a rationale for the absence of carbon loss by dissociation and desorption of the *t*-butyl group through DEA. At the surface, the energy dissipation is direct, and the dissociation process is likely to be dampened in the presence of alternative relaxation paths such as the bending motion in the current case.

4 Conclusions

In the context of the development of precursor molecules suitable for the fabrication of gold nanostructures through focused electron beam induced deposition, we have studied low energy electron-induced fragmentation of $CF_3AuCNC(CH_3)_3$. Dissociative electron attachment and dissociative ionization were studied both under single collision conditions and under conditions where collisional stabilization is provided. Dissociative ionization under single collision conditions was found to be more extensive than when collisional stabilization is provided and is dominated by charged organic ligand fragments, rather than charged gold-containing fragments, as is the case in the DIP EI MS experiments. Interestingly the electron attachment spectra are identical under both conditions, and dissociation of the initially formed TNI to form $[CF_3AuCN]^-$ is the only significant channel. We find that the parent anion has positive electron affinity and would thus rather expect stabilization and its observation where intermolecular energy dissipation is provided. However, comparison of the LUMO of the neutral parent molecule with that of the HOMO of the relaxed anion indicates a strong π^*–σ^* coupling in the attachment process, with a σ^* antibonding character along the observed dissociation coordinate. We thus anticipate that dissociative relaxation along this coordinate proceeds significantly faster than collisional stabilization and relaxation of the anion to its ground state. When comparing the current gas phase results with the composition of deposits from this precursor generated in electron-induced deposition in an UHV Auger spectrometer, marked differences are apparent. In the deposition experiments, the stoichiometric carbon and nitrogen content of the parent molecule is retained in the deposit, while the fluorine is almost quantitatively removed. From the gas phase experiments, on the other hand, significant carbon removal should be expected but only partial fluorine removal. Moreover, while the fluorine loss in the gas phase experiments is predominantly through dissociation of the CF_3 ligand, the fluorine removal in the deposit experiment is sequential through prolonged electron irradiation. In agreement with the deposition experiment, we attribute this to an initial fragmentation and immobilization on the surface through a first electron/molecule interaction. In this step, desorption, and in part also dissociation, is hindered through molecule surface interactions and efficient energy dissipation. Prolonged irradiation then leads to further fragmentation in electron-induced secondary and tertiary reactions that result in sequential fluorine loss, finally resulting in almost quantitative fluorine loss and carbonization of the remaining ligands.

Importantly, the consideration of the role of electron-induced secondary and tertiary reactions changes the parameter space that needs to be considered in the rational design of FEBID precursors and also has consequences for the deposition strategies applied. Specifically, potential precursors need to be designed in such a way that the immobilized fragments from the initial electron-induced dissociation processes are still susceptible to further electron-induced fragmentation, leading to desorption of the respective secondary ligand fragments.

Acknowledgements Thank you, Michael, for your friendship and good times and all your contributions to the electron molecule interaction community. This work received funding from the European Union's Horizon 2020 research and innovation program under the Marie Skłodowska-Curie Grant Agreement No. 722149. O.I. and A.K. acknowledge support from the Icelandic Centre of Research (RANNIS), Grant No. 185346-05. L.M.-W and W.G.C. thank the National Science Foundation for their support under Grant CHE-1904802. Support of MS instrumentation at the University of Florida was provided by the National Institutes of Health through the Grant S10 OD021758-01A1. The authors thank Dr. Ragnar Björnsson for constructive discussions during the preparation of the manuscript.

Author contributions

AK contributed to investigation, calculations, formal analysis, validation, writing—original draft, visualization. WGC

contributed to resources, investigation. JVJ contributed to resources, investigation. LM-W contributed to funding acquisition, conceptualization, supervision, resources, writing—review and editing. OI contributed to project administration, conceptualization, funding acquisition, supervision, writing—review and editing, methodology.

Data Availability Statement This manuscript has no associated data or the data will not be deposited. The datasets generated during and/or analyzed during the current study are available from the corresponding author on reasonable request.

References

1. K. Saha, S.S. Agasti, C. Kim, X. Li, V.M. Rotello, Gold nanoparticles in chemical and biological sensing. Chem. Rev. **112**(5), 2739–2779 (2012). https://doi.org/10.1021/cr2001178
2. L.A. Dykman, N.G. Khlebtsov, Gold nanoparticles in biology and medicine: recent advances and prospects. Acta Nat. **3**(2), 34–55 (2011). https://doi.org/10.32607/20758251-2011-3-2-34-56
3. X. Yang, M. Yang, B. Pang, M. Vara, Y. Xia, Gold nanomaterials at work in biomedicine. Chem. Rev. **115**(19), 10410–10488 (2015). https://doi.org/10.1021/acs.chemrev.5b00193
4. P. Sondhi, D. Lingden, J.K. Bhattarai, A.V. Demchenko, K.J. Stine, Applications of nanoporous gold in therapy, drug delivery, and diagnostics. Metals. (2023). https://doi.org/10.3390/met13010078
5. Y.-C. Yeh, B. Creran, V.M. Rotello, Gold nanoparticles: preparation, properties, and applications in bionanotechnology. Nanoscale **4**(6), 1871–1880 (2012). https://doi.org/10.1039/C1NR11188D
6. H. Hassan, P. Sharma, M.R. Hasan, S. Singh, D. Thakur, J. Narang, Gold nanomaterials—the golden approach from synthesis to applications. Mater. Sci. Energy Technol. **5**, 375–390 (2022). https://doi.org/10.1016/j.mset.2022.09.004
7. B.B. Oliveira, D. Ferreira, A.R. Fernandes, P.V. Baptista, Engineering gold nanoparticles for molecular diagnostics and biosensing. WIREs Nanomed. Nanobiotechnol. **15**(1), e1836 (2023). https://doi.org/10.1002/wnan.1836
8. M. Huth, F. Porrati, O.V. Dobrovolskiy, Focused electron beam induced deposition meets materials science. Microelectron Eng. (2017). https://doi.org/10.1016/j.mee.2017.10.012
9. R. Hu, L. Yu, Review on 3D growth engineering and integration of nanowires for advanced nanoelectronics and sensor applications. Nanotechnology (2022). https://doi.org/10.1088/1361-6528/ac547a
10. Y. Zhang, W. Chu, A.D. Foroushani, H. Wang, D. Li, J. Liu, C.J. Barrow, X. Wang, W. Yang, New gold nanostructures for sensor applications: a review. Materials (Basel) **7**(7), 5169–5201 (2014). https://doi.org/10.3390/ma7075169
11. M. Sackmann, S. Bom, T. Balster, A. Materny, Nanostructured gold surfaces as reproducible substrates for surface-enhanced Raman spectroscopy. J. Raman Spectrosc. **38**(3), 277–282 (2007). https://doi.org/10.1002/jrs.1639
12. M. Hu, J. Chen, Z.-Y. Li, L. Au, G.V. Hartland, X. Li, M. Marquez, Y. Xia, Gold nanostructures: engineering their plasmonic properties for biomedical applications. Chem. Soc. Rev. **35**(11), 1084–1094 (2006). https://doi.org/10.1039/B517615H
13. I. Utke, P. Hoffmann, J. Melngailis, Gas-assisted focused electron beam and ion beam processing and fabrication. J. Vac. Sci. Technol. B Microelectron. Nanom. Struct. **26**(4), 1197–1276 (2008). https://doi.org/10.1116/1.2955728
14. M. Huth, F. Porrati, C. Schwalb, M. Winhold, R. Sachser, M. Dukic, J. Adams, G. Fantner, Focused electron beam induced deposition: a perspective. Beilstein J. Nanotechnol. **3**(1), 597–619 (2012). https://doi.org/10.3762/bjnano.3.70
15. M. Huth, Focused electron beam induced deposition-principles and applications. Proc. Beilstein Symp. Funct. **25**, 193–212 (2010)
16. W.G. Carden, H. Lu, J.A. Spencer, D.H. Fairbrother, L. McElwee-White, Mechanism-based design of precursors for focused electron beam-induced deposition. MRS Commun. **8**(2), 343–357 (2018). https://doi.org/10.1557/mrc.2018.77
17. W.F. Van Dorp, C.W. Hagen, A critical literature review of focused electron beam induced deposition. J. Appl. Phys. (2008). https://doi.org/10.1063/1.2977587
18. I. Utke, A.P.R. Stanislav Moshkalev, *Nanofabrication Using Focused Ion and Electron Beams*; 2018.
19. W.G. Carden, J. Pedziwiatr, K.A. Abboud, L. McElwee-White, Halide effects on the sublimation temperature of X-Au-L complexes: implications for their use as precursors in vapor phase deposition methods. ACS Appl. Mater. Interfaces **9**(46), 40998–41005 (2017). https://doi.org/10.1021/acsami.7b12465
20. R.M. Thorman, T.P. Ragesh Kumar, D. Howard Fairbrother, O. Ingólfsson, The role of low-energy electrons in focused electron beam induced deposition: four case studies of representative precursors. Beilstein J. Nanotechnol. **6**(1), 1904–1926 (2015). https://doi.org/10.3762/bjnano.6.194
21. O. Ingólfsson, *Low-Energy Electrons Fundamentals and Applications* (Pan Stanford Publishing Pte. Ltd., Singapore, 2019)
22. S. Engmann, M. Stano, P. Papp, M.J. Brunger, Š Matejčík, O. Ingólfsson, Absolute cross sections for dissociative electron attachment and dissociative ionization of cobalt tricarbonyl nitrosyl in the energy range from 0 EV to 140 EV. J. Chem. Phys. **138**(4), 0–7 (2013). https://doi.org/10.1063/1.4776756
23. A. Kamali, E. Bilgilisoy, A. Wolfram, T.X. Gentner, G. Ballmann, S. Harder, H. Marbach, O. Ingólfsson, On the electron-induced reactions of $(CH_3)AuP(CH_3)_3$: a combined UHV surface science and gas-phase study. Nanomaterials (2022). https://doi.org/10.3390/nano12152727
24. J.D. Wnuk, J.M. Gorham, S.G. Rosenberg, W.F. Van Dorp, T.E. Madey, C.W. Hagen, D.H. Fairbrother, Electron beam irradiation of dimethyl-(acetylacetonate) Gold(III) adsorbed onto solid substrates. J. Appl. Phys. (2010). https://doi.org/10.1063/1.3295918

25. M.G. Jenke, D. Lerose, C. Niederberger, J. Michler, S. Christiansen, I. Utke, Toward local growth of individual nanowires on three-dimensional microstructures by using a minimally invasive catalyst templating method. Nano Lett. **11**(10), 4213–4217 (2011). https://doi.org/10.1021/nl2021448
26. A. Folch, High-vacuum versus "environmental" electron beam deposition. J. Vac. Sci. Technol. B Microelectron. Nanom. Struct. **14**(4), 2609 (1996). https://doi.org/10.1116/1.588994
27. H.W.P. Koops, J. Kretz, M. Rudolph, M. Weber, G. Dahm, K.L. Lee, Characterization and application of materials grown by electron-beam-induced deposition. Jpn. J. Appl. Phys. **33**(Part 1, No. 12B), 7099–7107 (1994). https://doi.org/10.1143/jjap.33.7099
28. M.M. Shawrav, P. Taus, H.D. Wanzenboeck, M. Schinnerl, M. Stöger-Pollach, S. Schwarz, A. Steiger-Thirsfeld, E. Bertagnolli, Highly conductive and pure gold nanostructures grown by electron beam induced deposition. Sci. Rep. (2016). https://doi.org/10.1038/srep34003
29. T. Brintlinger, M.S. Fuhrer, J. Melngailis, I. Utke, T. Bret, A. Perentes, P. Hoffmann, M. Abourida, P. Doppelt, Electrodes for carbon nanotube devices by focused electron beam induced deposition of gold. J. Vac. Sci. Technol. B Microelectron. Nanom. Struct. **23**(6), 3174–3177 (2005). https://doi.org/10.1116/1.2130355
30. A. Perentes, P. Hoffmann, F. Munnik. Focused electron beam induced deposition of gold and rhodium, in *23rd European Mask and Lithography Conference*, vol. 6533 (2007), p. 65331Q. https://doi.org/10.1117/12.736918
31. I. Utke, P. Hoffmann, B. Dwir, K. Leifer, E. Kapon, P. Doppelt, Focused electron beam induced deposition of gold. J. Vac. Sci. Technol. B Microelectron. Nanom. Struct. **18**(6), 3168 (2000). https://doi.org/10.1116/1.1319690
32. J.J.L. Mulders, J.M. Veerhoek, E.G.T. Bosch, P.H.F. Trompenaars, Fabrication of pure gold nanostructures by electron beam induced deposition with Au(CO)Cl precursor: deposition characteristics and primary beam scattering effects. J. Phys. D Appl. Phys. **45**(47), 1–8 (2012). https://doi.org/10.1088/0022-3727/45/47/475301
33. C. Glessi, A. Mahgoub, C.W. Hagen, M. Tilset, Gold(I) N-heterocyclic carbene precursors for focused electron beam-induced deposition. Beilstein J. Nanotechnol. **12**, 257–269 (2021). https://doi.org/10.3762/bjnano.12.21
34. W.G. Carden, R.M. Thorman, I. Unlu, K.A. Abboud, D.H. Fairbrother, L. McElwee-White, Design, synthesis, and evaluation of CF_3AuCNR precursors for focused electron beam-induced deposition of gold. ACS Appl. Mater. Interfaces **11**(12), 11976–11987 (2019). https://doi.org/10.1021/acsami.8b18368
35. E.H. Bjarnason, B. Ómarsson, S. Engmann, F.H. Ómarsson, O. Ingólfsson, Dissociative electron attachment to titatinum tetrachloride and titanium tetraisopropoxide. Eur. Phys. J. D (2014). https://doi.org/10.1140/epjd/e2014-50091-9
36. T. Fiegele, G. Hanel, I. Torres, M. Lezius, T.D. Märk, Threshold electron impact ionization of carbon tetrafluoride, trifluoromethane, methane and propane. J. Phys. B At. Mol. Opt. Phys. **33**(20), 4263–4283 (2000). https://doi.org/10.1088/0953-4075/33/20/306
37. W.G. Carden, Ligand Effects in Gold Precursors for Focused Electron Beam Induced Deposition. Ph.D. Dissertation, University of Florida (2020)
38. F. Neese, The ORCA program system. Wiley Interdiscip. Rev. Comput. Mol. Sci. **2**(1), 73–78 (2012). https://doi.org/10.1002/wcms.81
39. S. Grimme, R. Huenerbein, S. Ehrlich, On the importance of the dispersion energy for the thermodynamic stability of molecules. ChemPhysChem **12**(7), 1258–1261 (2011). https://doi.org/10.1002/cphc.201100127
40. K.P. Kepp, Benchmarking Density functionals for chemical bonds of gold. J. Phys. Chem. A **121**(9), 2022–2034 (2017). https://doi.org/10.1021/acs.jpca.6b12086
41. R. Kang, H. Chen, S. Shaik, J. Yao, Assessment of theoretical methods for complexes of Gold(I) and Gold(III) with unsaturated aliphatic hydrocarbon: which density functional should we choose? J. Chem. Theory Comput. **7**(12), 4002–4011 (2011). https://doi.org/10.1021/ct200656p
42. C. Riplinger, F. Neese, An efficient and near linear scaling pair natural orbital based local coupled cluster method. J. Chem. Phys. **138**(3), 34106 (2013). https://doi.org/10.1063/1.4773581
43. O. May, D. Kubala, M. Allan, Dissociative electron attachment to Pt(PF3)4—a precursor for focused electron beam induced processing (FEBIP). Phys. Chem. Chem. Phys. **14**(9), 2979–2982 (2012). https://doi.org/10.1039/C2CP23268E
44. S. Engmann, M. Stano, Š Matejčík, O. Ingólfsson, The role of dissociative electron attachment in focused electron beam induced processing: a case study on cobalt tricarbonyl nitrosyl. Angew. Chem. Int. Ed. **50**(40), 9475–9477 (2011). https://doi.org/10.1002/anie.201103234
45. P.Y. Shih, R. Tafrishi, M. Cipriani, C.F. Hermanns, J. Oster, A. Gölzhäuser, K. Edinger, O. Ingólfsson, Dissociative ionization and electron beam induced deposition of tetrakis(dimethylamino)silane, a precursor for silicon nitride deposition. Phys. Chem. Chem. Phys. **24**(16), 9564–9575 (2022). https://doi.org/10.1039/d2cp00257d
46. R.M. Thorman, P.A. Jensen, J.C. Yu, S.J. Matsuda, L. McElwee-White, O. Ingólfsson, D.H. Fairbrother, Electron-induced reactions of Ru(CO)4I2: gas phase, surface, and electron beam-induced deposition. J. Phys. Chem. C **124**(19), 10593–10604 (2020). https://doi.org/10.1021/acs.jpcc.0c01801

47. J.A. Spencer, Y.-C. Wu, L. McElwee-White, D.H. Fairbrother, Electron induced surface reactions of Cis-Pt(CO)2Cl2: a route to focused electron beam induced deposition of pure Pt nanostructures. J. Am. Chem. Soc. **138**(29), 9172–9182 (2016). https://doi.org/10.1021/jacs.6b04156
48. J.A. Spencer, J.A. Brannaka, M. Barclay, L. McElwee-White, D.H. Fairbrother, Electron-induced surface reactions of η3-allyl ruthenium tricarbonyl bromide [$(H_3C_3H_5)Ru(CO)_3Br$]: contrasting the behavior of different ligands. J. Phys. Chem. C **119**(27), 15349–15359 (2015). https://doi.org/10.1021/acs.jpcc.5b03775
49. Chemcraft—graphical software for visualization of quantum chemistry computations. https://www.chemcraftprog.com